Environ. Sci. Technol. **2009,** *43,* 6786–6792

Assessment of Long-Term Performance and Chromate Reduction Mechanisms in a Field Scale Permeable Reactive Barrier

BETTINA FLURY,[†] JAKOB FROMMER,[‡] URS EGGENBERGER,[†] URS MÄDER,[†,*] MAARTEN NACHTEGAAL,[§] AND RUBEN KRETZSCHMAR[‡]

Rock−Water Interaction Group, Institute of Geological Sciences, University of Bern, Switzerland, Institute of Biogeochemistry and Pollutant Dynamics, Department of Environmental Sciences, ETH Zürich, Switzerland, and Paul Scherrer Institute, General Energy Research Department, Laboratory for Energy and Materials Cycles, Villigen, Switzerland

Received December 11, 2008. Revised manuscript received May 13, 2009. Accepted May 14, 2009.

An innovative full-scale implementation of a permeable reactive barrier, consisting of a double-row of cylinders filled with zerovalent iron shavings, for chromate remediation was monitored over four years. Solid samples were analyzed to elucidate (i) the relevant corrosion mechanisms and products, (ii) the pathways of chromate reduction and immobilization, and (iii) the long-term performance of the barrier situated in a hydrological and geochemical complex groundwater regime. Sampling and analysis of groundwater and reactive material revealed an oxidative iron corrosion zone evolving in the inflow and a zone of anaerobic iron corrosion in the center and outflow of the barrier. Chromate reduction was mainly confined to the inflow region. The formation and thickness of corrosion rinds depended on sampling time, position, and depth, as well as on the size, shape, and graphite content. In the inflow, the corrosion rinds mostly consisted of goethite and ferrihydrite. X-ray absorption fine structure spectroscopy revealed two distinct Cr^{III} species, most likely resulting from homogeneous and heterogeneous redox reaction pathways, respectively. The longevity and long-term effectiveness of the PRB appears to be primarily limited by reduced corrosion rates of the ZVI-shavings because of the thick layers of Fe-hydroxides.

Introduction

Zerovalent iron (ZVI) is a highly reactive material that can be used for the remediation of contaminated groundwater. It is often applied in a permeable reactive barrier (PRB) system, in which contaminated subsurface water is forced to pass through a zone containing granular iron. Pilot and full-scale installations have demonstrated the success of ZVI-PRBs in removing organic and inorganic contaminants (*1*−*5*). The corrosion of ZVI results in the formation of redox-reactive interfaces and solution species, leading to reductive degradation of organic pollutants or immobilization of trace elements (e.g., Cr^{VI}, U^{VI}) by reduction. Despite its initial success some important challenges remain, including assessing the long-term performance (*6*), interferences with the hydrology (*1, 3*), and the need for more material- and cost-efficient strategies (*7*−*10*).

Predicting the long-term performance of PRBs and developing alternative approaches require an improved understanding of the geochemical processes involved in the contaminant treatment and of the influence of the groundwater chemistry on the PRB material. Little is known on whether processes identified in column studies apply to field scale installations (*3*).

A common application of ZVI-PRBs is the removal of mobile and toxic hexavalent chromium (Cr^{VI}, chromate) from groundwater by reduction to less soluble and less toxic Cr^{III}. Different pathways have been proposed for the reduction of chromate by ZVI, including a direct electron transfer from the metal surface (*11*), homogeneous solution phase reactions with Fe^{II} resulting from the metal corrosion, and heterogeneous reactions at the interface of neo-formed Fe^{II}-containing phases (*4*). One way to explore reaction pathways in complex field systems is to first asses the speciation of the reduced Cr^{III} and its association with other elements. This information is used to infer the relevant molecular mechanisms responsible for the formation of the Cr^{III} species observed (*4*). The required solid-state speciation data can be assessed by microfocused X-ray absorption fine-structure (XAFS) spectroscopy in a unique way at the micrometer scale.

In this study, we investigated reactive ZVI material sampled one to four years after installation of a PRB system designed to remediate a Cr^{VI} contaminated aquifer in Switzerland. The innovative design minimizes the amount of reactive material needed and partly relies on a dispersive Fe^{II}-plume extending the reductive capacity beyond the barrier itself. Furthermore, the installation allows a collection of solid samples and a monitoring of the groundwater chemistry at different locations within the barrier. In an accompanying study, the functionality of this installation has been shown (*12*).

The objectives of the present study were to (i) assess the state of the reactive material in this innovative PRB system with respect to the known problems of surface passivation and pore-space reduction and (ii) to examine the molecular−level mechanisms of the occurring corrosion and redox processes on the micrometer scale.

Information from the decameter scale (groundwater monitoring) to the molecular scale (XAFS) was integrated to cope with the complexity of this PRB system.

Materials and Methods

Study Site. The remediation site is located in Willisau, Switzerland, where copper-chromate solutions have been used in an industrial wood preservation process. From 1958 to 1987, hexavalent chromium seeped into the subsoil and accumulated in the unsaturated zone (*13*). The groundwater table considerably varies between 12−16 m depth (transition zone), and the aquifer thickness is 25 m. Groundwater velocity was established to be 5−6 m/day, which is rather high compared to most PRB settings (*12*). Contaminants accumulated in the unsaturated zone are leached into the groundwater and transported in flow direction of the groundwater with little vertical dispersion over several decameters. The groundwater chemistry at the site is dominated by calcium and bicarbonate with an electric

* Corresponding author address: Rock Water Interaction Group, Institute of Geological Sciences, University of Bern, Baltzerstrasse 3, 3012 Bern, Switzerland; phone: ++41 (0)31 631 45 63; fax: ++41 (0)31 631 48 43; e-mail:urs.maeder@geo.unibe.ch.

[†] University of Bern.

[‡] ETH Zürich.

[§] Paul Scherrer Institute.

10.1021/es803526g CCC: $40.75
Published on Web 07/24/2009

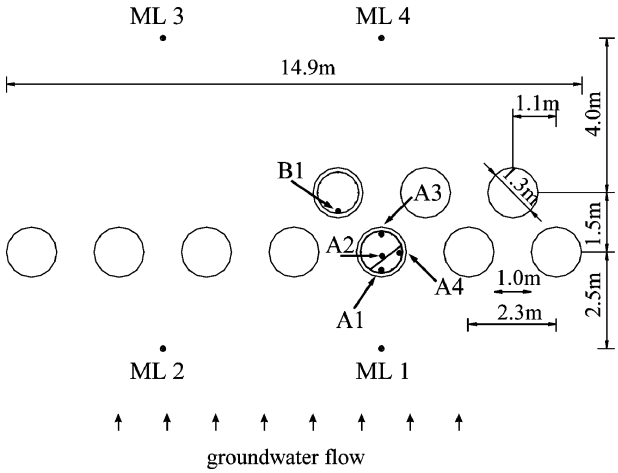

FIGURE 1. PRB Willisau in plan view as single and double row of cylinders filled with ZVI-shavings for chromate removal. ML1−ML4 are multilevel groundwater sampling wells. A1, A2, A3, A4, and B1 indicate positions of the MPSS within the cylinders. The individual piezometer bundles in A1−A4 and B1 each consists of four 1 in. piezometer (sampling of groundwater) and one 2 in. piezometer (sampling of solid material). A detailed description of the MPSS is given in ref *12*.

conductivity of 450−750 μS/cm, pH of 7.0−7.3, redox potential of 100−200 mV (relative to SHE), and dissolved ion concentrations of (in mg/L) HCO_3^-, ∼425; Ca^{2+}, 120−130; Mg^{2+}, 15−18; Na^+, 7.8−10.1; K^+, 1.4−2.2; Cl^-, 12−18; NO_3^-, 10.4−12.7; SO_4^{2-}, 19−40. Cr^{VI}-concentrations vary in the range of 0.0−2.5 mg/L. The dissolved oxygen content is medium to high at the site (3.5−6 mg/L) and varies with aquifer depth (5−6 mg/L in the transition zone and 3.5−5 mg/L at greater depth).

Reactive Barrier System. The permeable reactive barrier system in Willisau was constructed in an innovative design consisting of single and double rows of cylinders, respectively (Figure 1), filled with ZVI-shavings for chromate remediation. The cylinders are 1.3 m in diameter, and the filling depth extends from 12 to 23 m below land surface. A total of 233 t of reactive material was emplaced with a dry bulk density of 1.55 t/m^3 (*13*).

The reactive material is composed of a mixture of zerovalent cast-iron shavings (Gotthart Maier AG, Rheinfelden, Germany) and gravel in a ratio of 1:3 by volume. The shavings not only consist of pure iron (Fe, 92 wt %), but they also contain 2.8−3.2 wt % C and minor amounts of Si, P, Cr, Ni, Al, Cu, Zn, and Co. The shavings are 5−20 mm in length and possess graphite lamellae (size 10−80 μm). The gravel has a grain diameter of 2−5 mm and mainly consists of quartz (52 wt %), calcite (19 wt %), plagioclase (6 wt %), and K-feldspar (5 wt %). The rest is composed of mica, clay minerals, and accessory minerals. The mixture of Fe-shavings and gravel was chosen to prevent blocking of the pore space and to favor preferential flow of groundwater through the cylinders (*13*).

Sampling of Reactive Material. The monitoring of the PRB Willisau was performed using a specially designed multiport sampling system (MPSS) (SOLEXPERTS, Mönchaltorf, Switzerland). The MPSS-system enabled sampling at different levels of depths at several localities to get a three-dimensional understanding of the hydro-geochemical processes within the barrier (*12*). Two cylinders (referred to as A and B, respectively) of the double row are equipped with MPSS to access four levels of depth by individual piezometers (Figure 1). Level 1 (at 13.0−14.0 m depth) was always above the groundwater table. Level 2 (at 15.6−16.0 m depth) was situated in the transition zone. Levels 3 (at 18.1−19.1 m depth) and 4 (at 20.7−21.7 m depth) were located below the groundwater table. Cylinder A allowed sampling at different positions relative to groundwater flow: A1 (inflow), A2 (center), A3 (outflow), and A4 (lateral inflow).

The MPSS is attached to a reinforcement cage and consists at each position of an individual piezometer bundle of four 1 in. piezometers for sampling groundwater and one 2 in. piezometer for sampling reactive material. During installation of the cylinders a small amount of the reactive material was filled into stainless steel wire-mesh cages and positioned at levels corresponding to the groundwater sampling depths and separated by inflatable packers (Figure S1, Supporting Information).

For a detailed characterization of the reactive material, sampling was performed annually since the installation of the barrier in November 2003 (September 2004, Mai/September 2005, June 2006, October 2007). For this purpose, the wire-mesh cages were pulled out and opened to collect some reactive material and reinserted. For transport to the lab, the samples were immediately vacuum-sealed and kept at temperatures below 4 °C. In the lab, the samples were freeze-dried for further preparation.

Mineralogy, Metal Speciation, and Microbiologic Identification. Mineralogy and elemental composition of the corrosion rinds were characterized using a combination of X-ray diffraction (XRD), Raman spectroscopy, scanning electron microscopy (SEM), and X-ray fluorescence (XRF) (synchrotron and bench instrument). X-ray absorption near edge structure (XANES) spectra (*14*) were analyzed to determine the speciation (including the oxidation state) of Fe and Cr. Organic matter was further investigated by optical microscopy to identify possible biofilm formation.

For SEM, the iron shavings were embedded in a two-component epoxy resin (Epotex, Polyscience) and prepared as polished sections (3−5 mm thick). The analyses were conducted on a Zeiss-EVO50 scanning electron microscope coupled with an energy dispersive spectrometer (EDS). The acceleration voltage of the electron beam was set to 15 kV. Images were acquired using secondary and backscattered electron detectors. For μ-XRF and μ-XANES analysis, samples (gravel and Fe-shavings) were shock frozen in liquid nitrogen and freeze-dried. The samples were impregnated with a high purity resin (Epofix, Struers) and prepared as polished thin-sections (∼30 μm thick) on glass slides. μ-XRF measurements were carried out with an Eagle-II μProbe (Röntgenanalytik Messtechnik GmbH, Taunusstein, Germany), providing a beamsize of approximately 40 μm on the sample placed in a vacuum (∼30 mbar), allowing the detection of low-Z elements (Z > 11; e.g., Mg, Al, Si). The majority of the synchrotron based μ-XAFS and μ-XRF analyses were conducted at beamline 10.3.2 at the Advanced Light Source (ALS, Berkeley) using a seven-element Ge-detector. Technical details regarding the setup are published elsewhere (*15*). Additional work was done at the X05LA (μ-XAS) beamline at the Swiss Light Source (SLS), Paul Scherrer Institut, Villigen (Switzerland), and at beamline A1 at the Hamburger-Synchrotronstrahlungslabor (HASYLAB, Germany).

Additional details on the preparation of reference materials, experimental procedures for XRF and XAFS-spectroscopy, sample processing and measurement settings by XRD and Raman spectroscopy and microbiological identification of organic matter are provided in the Supporting Information.

Results and Discussion

Geochemical Conditions within the Barrier. Different discoloration of the wire-mesh cages and the reactive material indicated different geochemical conditions depending on locality and depth within the barrier cylinders. Generally, the reactive material had red coatings at the inflow of the cylinders, suggesting oxidizing conditions. In contrast, the reactive material appeared black at the center and the outflow

of the cylinders, indicating reducing conditions. The observed pattern changed over time (4 years), such that the reduced zone slowly got overprinted by red coating, and the weakly developed red coatings changed into more distinct red coatings. This alteration mainly took place near the inflow of the cylinder and at the depth of level 2 (transition zone). These visual characteristics of the reactive material were in line with the groundwater monitoring at these locations over the time span of four years (*12*): Reducing conditions (no Cr^{VI}, O_2, NO_3, SO_4; Fe^{II} present) slowly changed to oxidizing conditions (no Fe^{II}; Cr^{VI}, O_2, NO_3, SO_4 present). Oxidizing conditions dominated close to the transition zone and at the cylinders' inflow where the oxygen concentrations are the highest.

Investigation of Corrosion Rinds. The zerovalent iron shavings collected from the cylinders were always entirely covered by corrosion coatings, with the metallic iron core never exposed directly to the surface. As an example, Figure 2a shows a backscattered electron SEM image of a typical iron shaving sampled at the inflow position (A1) at depth level 3, featuring enhanced corrosion along cracks and fissures. Visual inspection of 30 samples suggested that the morphology and thickness of the corrosion rinds varied systematically with position and depth, size, and shape of the shavings, amount of graphite lamellae in the shavings, and elapsed time after installation of the PRB. The thickness of the corrosions rinds (*R*) perpendicular to the iron shaving and the width of the shaving (*S*) were semiquantitatively determined (Figure 2a) and expressed as percentage of corroded iron ($\%_{corr}$).

Maximum corrosion of the iron shavings was found in the inflow positions of the cylinders, both for the front (A1) and back (B1) row (Figure 1). Modest corrosion was observed in the center (A2) and minimal corrosion in the outflow (A3) positions of the cylinder. Comparing the iron shavings collected at different sampling depths revealed that the degree of corrosion was strongest at the depth of the fluctuating groundwater table (level 2). At greater depths the degree of corrosion clearly decreased, which can be explained by the lower oxygen concentrations in the groundwater below the transition zone (3.5−5 mg/L O_2) compared to the transition zone (5−6 mg/L O_2).

Small shavings with many cracks and fissures, as shown in Figure 2a, generally appeared more corroded than larger and more compact shavings. Furthermore, graphite lamellae in the shaving lead to brittleness and fracturing. Consequently, shavings with graphite lamellae featured thicker corrosion rinds. Preferred oxidation of ZVI along graphitic inclusions has been previously observed in laboratory studies (*7*). Figure 2 shows backscattered electron SEM images of the direct inflow position of the front (A1) and the back row (B1) at levels 2 and 3, respectively. Clearly visible are unaffected graphite lamellae within the ZVI-core and residual lamellae within the corrosion rinds. Corrosion preferentially initiated along lamellae that were in direct contact with the corrosion rim.

The extent of corrosion slightly increased with the time elapsed since the installation of the reactive barrier in 2003. For example, at the inflow position (A1 and B1) at the depth of level 2, the ratio between corrosion rinds and shaving width increased from ~10% to 10−20% within four years.

Characterization of Samples from the Reduced Zone. Backscattered electron SEM images showed thin and relatively homogeneous corrosion rinds around iron shavings (data not shown) originating from the primarily reduced parts of the barrier (center A2, levels 3, 4; outflow A3, levels 2, 3, 4). Representative μ-XRF maps of material sampled in the reduced and oxidized zones are shown in Figure S2, Supporting Information. Markedly higher calcium and sulfur counts and only few (level 2) to no Cr counts (levels 3 + 4)

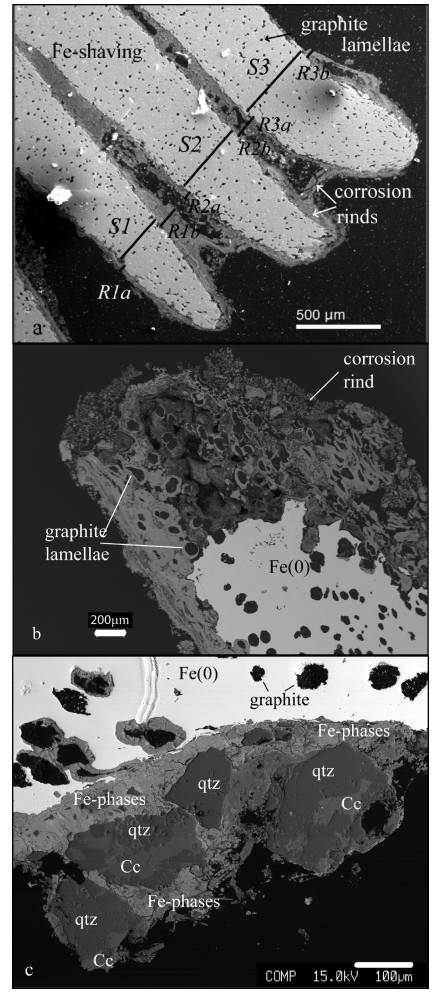

FIGURE 2. Backscattered electron SEM images (black = epoxy resin; light gray = zerovalent iron; dark gray = other mineral phases). (a) Irregular formed and partially corroded iron shaving. Secondary phases preferentially precipitated along cracks and fissures. S1−S3: Shaving width. R1a/b−R3a/b: Thickness of corrosion rinds. Sampled in Mai 2005, position A1, level 3. (b) Heavily corroded part of ZVI-shaving consisting of mostly Fe-(hydr)oxides. Graphite lamellae are still visible. Sampled in June 2006, position A1, level 2. (c) Grains of quartz (qtz) and carbonate (Cc) embedded into the Fe-(hydro)oxides rich matrix of the corrosion crust (Fe-phases). Corrosion also occurs around graphite lamellae where they are in direct contact with the surface of the shaving. Sampled in June 2006, position B1, level 2.

were determined for the reduced zone. Ca and S were homogeneously distributed in a thin layer around the shavings and no apparent cluster-formation was observed. XRD-analyses of the corrosion rinds revealed graphite as the only detectable phase (~3 wt % C graphite was originally contained in the cast iron). The occurrence of S in the thin Fe corrosion layers (Figure S2, Supporting Information) suggests the precipitation of Fe sulfides. Analyses of the groundwater chemistry upstream, within and downstream of the barrier showed a decrease in dissolved Ca from ~120 mg/L to 80−90 mg/L mainly in the back part of the cylinder. This loss of Ca is associated with carbonate precipitation as a mechanism for buffering the pH increase resulting from iron oxidation and sulfate/nitrate/chromate reduction. Assuming a groundwater flux of 900 L/m^2/day (flow velocity of 6 m/d, aquifer porosity of 0.15 (*13*)), the precipitation results in ~80 g/m^2/day of $CaCO_3$ or 30 kg/m^2/year. To calculate the approximate pore space infilling we assume that the precipitation occurs along a flow path of 1 m (i.e., roughly two-

third of the cylinder). Under this assumption, 2.2% of the available pore-space (initially 50% within the cylinders) in this region is lost per year because of the precipitation of $CaCO_3$.

Characterization of Samples from the Oxidized Zone. The surface of particles sampled from the oxidized zone of the PRB (inflow positions A1 and B1) was characterized by a diversity of deposited particulates, corrosion products, and precipitated phases in proximity to each other (Figure 2). The corrosion rinds consisted of an Fe-(hydr)oxide matrix often enclosing grains of either Ca-carbonates or silicate minerals. The latter were identified as feldspar or quartz. The inhomogeneous distribution of Si (data not shown) and Ca (Figure S2, Supporting Information) together with the crystal morphology as assessed by SEM show that the majority of the Ca-carbonates and silicates in the inflow were not precipitated within the barrier but are deposited particles originating from the gravel additive (*4, 16*). Additionally, SEM examinations indicated the formation of new calcite crystals e.g. in the form of needles (Figure S4, Supporting Information).

The predominant Ca-carbonate phase was calcite. S was only occasionally observed within the rinds of shavings of the oxidized zone (Figure S2, Supporting Information).

After two years of operation the accumulation of a reddish biofilm containing the iron-oxidizing bacteria *Gallionella ferruginea* (Figure S5, Supporting Information) was observed. The build-up of bacterial biomass was small (visual observation) and was confined to the inflow of the cylinders. Thus, its adverse impact on the operation of the PRB (clogging effects and biofouling (*1*)) is assumed to be negligible.

Iron Speciation. The following discussion of the metal (Fe and Cr) speciation is restricted to samples from the zone of aerobic iron corrosion. Several phases can be distinguished in the SEM-images by their different backscattered electron intensity, caused by the mean atomic density of the material, and their shape (blocky, needles, platelets). All microanalytical methods revealed a heterogeneous mineralogy and chemical composition, which is indicative of locally varying chemical conditions. Fe K-edge μ-XANES-spectra were recorded on samples of the oxidized zone at various points of interest (POI). The spectrum Fe-POI1 (Figure 3) is representative for the speciation of Fe in the corrosion crusts. On average, Fe occurred in a mixture of goethite (~60%) and ferrihydrite (~30%) (both are Fe^{III}-oxyhydroxides) containing a small fraction (~10%) of Fe^{II} (linear combination fitting results, Figure 3). In addition, hematite and maghemite were occasionally detected by Raman spectroscopy. XRD analysis suggested magnetite ($Fe^{II}Fe^{III}_2O_4$) as the major Fe^{II}-phase and confirmed the presence of goethite and ferrihydrite (data not shown). The XRD patterns additionally contained small contributions from lepidocrocite, which is not easily distinguished from goethite in complex systems by the use of XANES-spectroscopy alone. The results of XRD, XANES-, and Raman-spectroscopy consistently suggested the corrosion crusts being composed of amorphous and crystalline Fe^{III}-hydroxides interspersed with some Fe^{II} containing phases (magnetite). The surfaces of the gravel additive in the oxidized zone were also coated with brown precipitates. For these crusts (Figure S6, Supporting Information), a similar mineralogical composition for Fe was determined (data not shown). A striking exception to this pattern, though far less abundant, were strongly weathered regions on the Fe-shavings extending up to some 100 μm into the Fe-core (Figure 3; left side of the ZVI shaving). For these regions μ-XANES-spectroscopy unequivocally showed the almost exclusive occurrence of siderite (Figure 3: spectrum Fe-POI2) and a gradual change to metallic Fe (Figure 3: spectrum Fe-POI3) as the iron core was approached.

The mineralogy of the corrosion crust is in agreement with findings reported in the literature (*4, 10, 17*). The

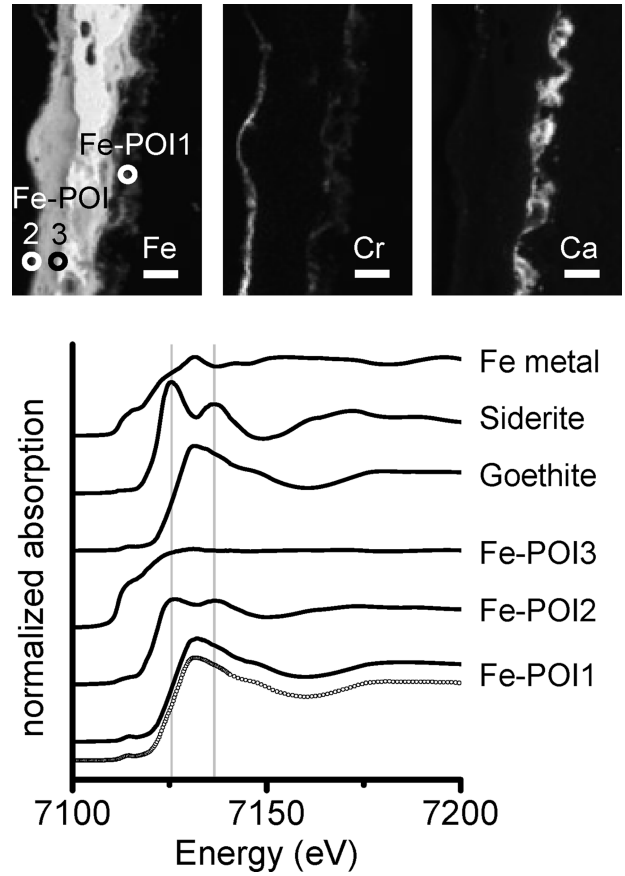

FIGURE 3. Synchrotron μ-XRF distribution maps of Fe, Cr, and Ca around a ZVI-shaving sampled at the inflow of the back-cylinder (B1; level 2; scale bar = 200 μm) and Fe K-edge μ-XANES spectra of the POIs (point of interest) indicated in the map (dark = low concentrations; light = high concentrations). Fe-POI3 (metallic Fe) is strongly distorted due to "over-absorption" caused by the high Fe concentration (*33*). Three relevant reference spectra measured in transmission mode are shown for comparison. For Fe-POI1 the linear combination fit results (dotted line, ferrihydrite 30%; goethite 60%; siderite 3%; magnetite 7%) are shown.

predominance of Fe^{III}-hydroxides can be explained by the continuous supply of oxygen in the upstream groundwater and the variation in the groundwater table causing periodically oxic conditions in the transition zone.

Chromium Speciation. The μ-XRF mapping (Figures 4, S2, Supporting Information, and S6, Supporting Information) of samples from the inflow positions (A1, B1) showed low and rather homogeneously distributed Cr-concentrations within the corrosion crusts (but not extending to the Fe-core) and on the surface of the gravel particles. In contrast, Cr-enrichments were found at the edges of the corrosion coatings (Figure 3; left side of the ZVI shaving) and along irregular structures of unknown origin (Figure 4). These two different distribution patterns were also associated with a different Cr speciation. Twenty-one μ-XANES-spectra were measured at selected POIs. The evenly distributed Cr in the corrosion crust is best represented by the XANES-spectrum of Cr-POI1 (Figure 4) and Cr in the Cr-enrichments by the spectrum of Cr-POI2. There was no detectable Cr^{VI} in any of the samples as indicated by the absence of a pre-edge peak at 5993 eV (*18*). Our observed XANES-spectra differed from reported spectra of Cr substituted goethite (*19*) and of Cr_2O_3 (*16*) but agreed well with the spectral features of mixed Cr^{III}–Fe^{III}-hydroxides (*20, 21*). For these hydroxides a relation between the molar fraction of Cr and specific extended XAFS (EXAFS) features has been suggested recently (*21*). The rather

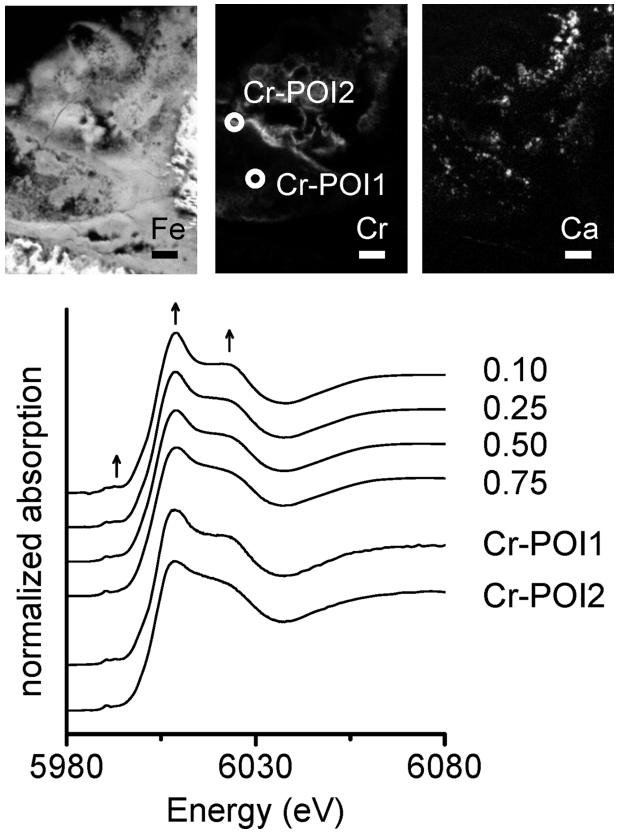

FIGURE 4. Synchrotron μ-XRF distribution maps of Fe, Cr, and Ca around a zerovalent iron shaving sampled at the inflow of the back-cylinder (B1; level 2; scale bar = 200 μm) and Cr K-edge μ-XANES spectra of the POIs indicated in the map (dark = low concentrations; light = high concentrations). Bulk Cr-XANES spectra of $Cr^{III}-Fe^{III}$-hydroxide references are shown with the molar Cr/(Fe+Cr) ratio indicated by numbers. Arrows indicate principal spectral changes. Enlarged views of the pre-edge spectra of the POIs and the synthetic references are shown in Figure S3, Supporting Information.

low Cr-concentrations in parts of the corrosion crusts prevented a systematic Cr-EXAFS investigation of our samples. However, Figure 4 shows that also the XANES spectra of synthesized $Cr^{III}-Fe^{III}$-hydroxides with varying Cr/Fe ratios exhibited systematic differences: the spectra of the reference with small Cr/Fe differ from the samples with high Cr/Fe by a more intense prepeak at 5992.7 eV (Figure 4c), a smaller, more intense whiteline and a more pronounced shoulder in the postedge. The variation observed for the reference compounds and comparison with published spectra (*22*) led us to interpret the different μ-XANES spectra found for different POIs in terms of different Cr/Fe ratios in a semiquantitative way. Consequently, the molecular Cr/Fe ratio was close to 1/3 in regions with low and homogeneously distributed Cr-concentrations (Cr-POI1), while it was considerably larger in regions enriched with Cr (Cr-POI2) (Figure 4). The average composition of the solid was determined from the semiquantitative ratio of the X-ray fluorescence lines (i.e., ignoring matrix attenuation of the fluorescence radiation). The μ-XRF-analysis indicated on average Cr/Fe ratio <0.1 (Figure S6, Supporting Information). This discrepancy between the μ-XANES results and the μ-XRF data is likely attributed to the proximity of Fe^{III}-hydroxides and of mixed $Cr^{III}-Fe^{III}$-hydroxides (sample fluorescence is related to the average composition of the volume penetrated by the X-ray, while Cr-XANES specifically probes the direct molecular environment of Cr).

Redox Processes. The Cr/Fe ratio in the immediate coordination environment around Cr has been shown to differ in precipitates resulting from homogeneous and heterogeneous redox reactions, respectively. While homogeneous reactions between Fe^{II} and Cr^{VI} result in the formation of mixed $Cr^{III}-Fe^{III}$-hydroxides with a Cr/Fe ratio of around 1/3 (*21, 23*), the formation of Cr rich clusters (i.e., Cr/Fe exceeding 1/3) results from electron transfer reactions involving Cr^{VI} and Fe^{II} either bound to surfaces (*24*) or bound in redox-reactive phases (e.g., green rust (*25*),). Thus, the occurrence of two different Cr^{III} species (in terms of the molecular Cr/Fe ratio) in the corrosion crust of the ZVI shavings indicates two effective reaction pathways: The Cr species in the Cr-enriched areas (molecular Cr/Fe ratio >1/3) appears to result from heterogeneous redox reactions (involving Fe^{II} bearing solids) whereas the evenly distributed Cr (connected to a molecular Cr/Fe ratio of about 1/3) seems to result from homogeneous reactions with dissolved Fe^{II}. The occurrence of $Cr^{III}-Fe^{III}$-hydroxides on the surface of the gravel additives further suggest that homogeneous oxidation of Fe^{II}, either by oxygen or by Cr^{VI}, also occurs within the pore space. Fe^{III}-hydroxide colloids formed in the solution phase are deposited subsequently. The proposed homogeneous pathway in the pore space involves the co-occurrence of Fe^{II} with Cr^{VI} and oxygen in the solution phase, despite the short half-life of Fe^{II} in neutral oxygenated or Cr^{VI} containing waters. This delayed oxidation of Fe^{II} may be caused by kinetic control at low O_2 and Cr^{VI} concentrations. Alternative explanations include different transport paths for oxidants and Fe^{II} or spatiotemporal variations of the redox-conditions within the crust (shifting anodic and cathodic sites (*26*), patches of high microbial activity, etc.).

The quantitative significance and possible temporal sequences of the two hypothesized reaction pathways (homogeneous and heterogeneous reduction) in the oxidized zone need to be addressed in more controlled environments. Both mechanisms result in the formation of $Cr^{III}-Fe^{III}$-hydroxides with a Cr-solubility far below critical limits ($\log[Cr^{3+}] < -7$ at pH = 7 (*27*)). The microanalytical findings (i.e., Cr-containing precipitates on the gravel surfaces and solids with a Cr/Fe ratio of 1/3 in the corrosion rinds) strongly suggest that, as intended in the design process, homogeneous Cr^{VI} reduction is an important pathway within the zone impacted by ZVI corrosion. Homogeneous reactions may also take place in the mixing zone between the Fe^{II} plume formed in the back parts of the cylinders (see below) and flowpaths initially bypassing the reactive media (*12*).

The formation of a stable Fe^{II} plume as observed downstream of the barrier (*12*), is not expected to form until CrO_4^{2-}, O_2, and NO_3^-, readily reacting with Fe^{II}, are significantly diminished. The Fe^{II} plume thus evolves as a result of anaerobic Fe^0 corrosion in the reducing zone (i.e., in the back part of the cylinders). Iron shavings from this zone are surrounded by thin corrosion layers containing Ca, Fe, and S (Figure S2, Supporting Information). The close association of Fe and S suggests the occurrence of Fe-sulfides. As abiotic sulfate reduction is very slow at aquifer temperatures (*28*), the precipitated sulfide is most likely produced by sulfate reducing microorganisms consuming hydrogen from the anaerobic iron corrosion (*17*). In addition, the occurrence of other Fe^{II} bearing secondary precipitates (like magnetite) can not be excluded. Hardly any Cr was detected in these Ca−Fe−S-crusts. Hence, reduction of Cr^{VI} on the surface of sulfides was of minor importance at our site, because enough reductive capacity is provided under normal conditions in the inflow zone. Therefore only negligible amounts of Cr^{VI} enter the zone dominated by sulfides.

Implications for the Long-Term Performance. To ensure a long-term efficiency of the installation the porosity of the reactive media and its reductive capacity needs to be

maintained (*1, 3, 17*). After four years of operation, the reactive material sampled at the Willisau site remained mostly unconsolidated (*12*). Our microscopic investigations suggested that the corrosion rinds are formed by two mechanisms: (i) the transformation from Fe^0- to Fe^{III}-phases resulted in a replacement of the zerovalent iron shaving with Fe-(hydr)oxides associated with a volume increase (3−4 times in case of total transformation of Fe^0 to goethite or ferrihydrite (*17*)). The corrosion rinds were additionally enlarged by (ii) embedding small particles and/or newly formed carbonate precipitates in the Fe^{III}-(hydr)oxide-matrix (Figure 2c and Figure S4, Supporting Information). Because the bulk of the shavings were not heavily corroded, the pore space infilling because of the precipitation of Fe-(hydr)oxides was small. Also significant pore space reduction by carbonate precipitation does not seem to be a problem in Willisau at present, most likely because of the ZVI/gravel-barrier in Willisau only showing a minor pH-increase (from pH ∼7.0 to ∼7.3 (*12*)) in comparison to massive granular ZVI-barriers. Clogging by organic matter is negligible because of the only marginal build-up of bacterial biomass at the inflow of the cylinders. In summary, the reduction of pore space in the reactive media due to organic and inorganic solids appears to be minor after four years of operation. Recent studies suggested that also the formation of gas bubbles may decrease the hydraulic conductivity of the reactive media (*29*). This aspect has not been investigated in the present study as until to date there was no indication for gas formation within the barrier (*12*). Thus, no adverse effect on the hydraulic conductivity is expected.

Passivating effects have been attributed to dense precipitate layers covering the ZVI surface and influencing the (mass) transport of Fe^{II} released at the anodic sites (*13, 30*). In addition, the electric conductivity of the precipitate layer has been shown to become rate limiting in case of dominating cathodic reactions occurring on the outermost precipitate-solution interface (*31*). In contrast, precipitate layers rich in poorly crystalline Fe^{III}-hydroxides, as primarily observed in the oxidized zone, are expected to interfere much less with the ZVI corrosion (*32*). Still, we observed geochemical changes within the cylinders: over four years, the oxygen concentration measured at the inflow of the barrier constantly increased and finally Cr^{VI} was detected within the first few cm of the cylinders (*12*). This observation indicates that the reduction rates which can be sustained by the corrosion of the ZVI shavings declined over time. This decline occurred although only a small portion of the total Fe^0 was oxidized. Thus, also under conditions promoting the formation of less passivating Fe^{III}-hydroxides, the resulting Fe^{III}-hydroxides formed at the ZVI surface will diminish the reductive capacity of the ZVI. As also found for the case of dense precipitate layers (*31*) we therefore conclude that predicting the lifetime of the PRB solely on the basis of the total Fe^0-content is inappropriate even if the ZVI is covered by less passivating poorly crystalline Fe^{III}-hydroxides.

Acknowledgments

This manuscript greatly benefited from the comments and suggestions by Dr. D. Dzombak and three anonymous reviewers. We gratefully acknowledge the support by the Swiss Federal Office for the Environment (FOEN) (Rubrik-Nr. 810.3189.044), the Geologische Beratungen Schenker, Korner & Partner GmbH, Luzern, and the Imprägnierwerk Willisau. We acknowledge the ALS, the HASYLAB, and the SLS for provision of synchrotron radiation facilities. The ALS is supported by the Director, Office of Science, Office of Basic Energy Sciences, of the U.S. Department of Energy under Contract No. DE-AC02-05CH11231. Drs. Andreas Voegelin (ETH Zurich), Camelia Borca, Daniel Grolimund (both PSI), Edmund Welter (HASYLAB), and Matthew A. Marcus (ALS) are acknowledged for help during XAFS data acquisition and discussions. S. Brechbühl (University of Bern) and A. Villard (University of Neuchâtel) prepared the resin-impregnated sections.

Supporting Information Available

Further details on the preparation of reference samples, the analysis of solid samples, instrumentation, additional SEM and XRF data, and methodology. This material is available free of charge via the Internet at http://pubs.acs.org.

Literature Cited

(1) Burmeier, H.; Birke, V.; Ebert, M.; Finkel, M.; Rosenau, D.; Schad, H. *Anwendung von durchströmten Reinigungswänden zur Sanierung von Altlasten*; Universität Lüneburg, Fakultät III (Umwelt und Technik): Suderburg, Germany, 2006.

(2) U.S. Environmental Protection Agency. *Capstone Report on the Application, Monitoring, And Performance of Permeable Reactive Barriers for Groundwater Remediation: Volume 2. Long-Term Monitoring of PRBs: Soil and Groundwater Sampling.* EPA/600/R-03/045b; U.S. EPA: Washington DC, 2003.

(3) Naftz, D. L.; Morrison, S. J.; Davies, J. A.; Fuller, C. C. *Handbook of Groundwater Remediation Using Permeable Reactive Barriers*; Elsevier Science: San Diego, CA, 2002.

(4) Wilkin, R. T.; Su, C. M.; Ford, R. G.; Paul, C. J. Chromium-removal processes during groundwater remediation by a zerovalent iron permeable reactive barrier. *Environ. Sci. Technol.* **2005**, *39*, 4599–4605.

(5) Scherer, M. M.; Richter, S.; Valentine, R. L.; Alvarez, P. J. Chemistry and microbiology of permeable reactive barriers for in situ groundwater clean up. *Crit. Rev. Environ. Sci. Technol.* **2000**, *30*, 363–411.

(6) Henderson, A. D.; Demond, A. H. Long-Term Performance of Zero-Valent Iron Permeable Reactive Barriers. *Crit. Rev. Environ. Eng. Sci.* **2007**, *24*, 401–423.

(7) Jeen, S.-W.; Jambor, J. L.; Blowes, D. W.; Gillham, R. W. Precipitates on Granular Iron in Solutions Containing Calcium Carbonate with Trichloroethene and Hexavalent Chromium. *Environ. Sci. Technol.* **2007**, *41*, 1989–1994.

(8) Kamolpornwijit, W.; Liang, L.; Moline, G.; Hart, T.; West, O. R. Identification and Quantification of Mineral Precipitation in Fe0-Filings from a Column Study. *Environ. Sci. Technol.* **2004**, *38*, 5757–5765.

(9) Kohn, T.; Livi, K. J.; Roberts, A. L.; Vikesland, P. J. Longevity of Granular Iron in Groundwater Treatment Processes: Corrosion Product Development. *Environ. Sci. Technol.* **2005**, *39*, 2867–2879.

(10) Phillips, D. H.; Watson, D. B.; Roh, Y.; Gu, B. Mineralogical Characteristics and Transformations during Long-Term Operation of a Zerovalent Iron Reactive Barrier. *J. Environ. Qual.* **2003**, *32*, 2033–2045.

(11) Liu, T.; Tsang, D. C. W.; Lo, I. M. C. Chromium(VI) Reduction Kinetics by Zero-Valent Iron in Moderately Hard Water with Humic Acid: Iron Dissolution and Humic Acid Adsorption. *Environ. Sci. Technol.* **2008**, *42*, 2092–2098.

(12) Flury, B.; Eggenberger, U.; Mäder, U. First Results of Operating and Monitoring an Innovative Design of a Permeable Reactive Barrier for the Remediaton of Chromate Contaminated Groundwater. *J. Appl. Geochem.* **2009**, *24* (4), 687–697.

(13) Köhler, S. ; ETH Zürich, Nr. 15453, 2003; p 177 (http://e-collection.ethbib.ethz.ch/view/eth:27382).

(14) Peterson, M. L.; Brown, G. E.; Parks, G. A.; Stein, C. L. Differential Redox and Sorption of Cr(III/VI) on Natural Silicate and Oxide Minerals: EXAFS and XANES Results. *Geochim. Cosmochim. Acta* **1997**, *61*, 3399–3412.

(15) Marcus, M. A.; MacDowell, A. A.; Celestre, R.; Manceau, A.; Miller, T.; Padmore, H. A.; Sublett, R. E. Beamline 10.3.2 at ALS: A Hard X-ray Microprobe for Environmental and Materials Sciences. *J. Synchrotron Radiat.* **2004**, *11*, 239–247.

(16) Phillips, D. H.; Gu, B.; Watson, D. B.; Roh, Y. Impact of Sample Preparation on Mineralogical Analysis of Zero-Valent Iron Reactive Barrier Materials. *J. Environ. Qual.* **2003**, *32*, 1299–1305.

(17) U.S. Environmental Protection Agency. *Capstone Report on the Application, Monitoring, And Performance of Permeable Reactive Barriers for Ground-Water Remediation: Volume 1. Performance Evaluations at Two Sites*; EPA/600/R-03/045a; U.S. EPA: Washington DC, 2003.

(18) Huggins, F. E.; Najih, M.; Huffman, G. P. Direct Speciation of Chromium in Coal Combustion By-Products by X-ray Absorption Fine Structure Spectroscopy. *Fuel* **1999**, *78*, 233–242.

(19) Sileo, E. E.; Ramos, A. Y.; Magaz, G. E.; Blesa, M. A. Long-Range vs Short-Range Ordering in Synthetic Cr-Substituted Goethites. *Geochim. Cosmochim. Acta* **2004**, *68*, 3053–3063.
(20) Manning, B. A.; Kiser, J. R.; Kwon, H.; Kanel, S. H. Spectroscopic Investigation of Cr(III)- and Cr(VI)-Treated Nanoscale Zerovalent Iron. *Environ. Sci. Technol.* **2007**, *41*, 586–592.
(21) Hansel, C. M.; Wielinga, B. W.; Fendorf, S. R. Structural and Compositional Evolution of Cr/Fe Solids after Indirect Chromate Reduction by Dissimilatory Iron-Reducing Bacteria. *Geochim. Cosmochim. Acta* **2003**, *67*, 401–412.
(22) Vikesland, P. J.; Valentine, R. L. Iron Oxide Surface-Catalyzed Oxidation of Ferrous Iron by Monochloramine: Implications of Oxide Type and Carbonate on Reactivity. *Environ. Sci. Technol.* **2002**, *36*, 512–519.
(23) Eary, L. E.; Rai, D. Chromate Removal from Aqueous Waters by Reduction with Ferrous Iron. *Environ. Sci. Technol.* **1987**, *22*, 972–977.
(24) Grolimund, D.; Trainor, T. P.; Fitts, J. P.; Kendelewicz, T.; Liu, P.; Chambers, S. A.; Brown, G. E. Identification of Cr Species at the Aqueous Solution−Hematite Interface after Cr(VI)−Cr(III) Reduction using GI-XAFS and Cr L-Edge NEXAFS. *J. Synchrotron Radiat.* **1999**, *6*, 612–614.
(25) Bond, D. L.; Fendorf, S. Kinetics and Structural Constraints of Chromate Reduction by Green Rusts. *Environ. Sci. Technol.* **2003**, *37*, 2750–2757.
(26) Powel, R. M.; Puls, R. W.; Hightower, S. K.; Sabatini, D. A. Coupled Iron Corrosion and Chromate Reduction: Mechanisms for Subsurface Remediation. *Environ. Sci. Technol.* **1995**, *29*, 1913–1922.
(27) Rai, D.; Sass, B. M.; Moore, D. A. Chromium(III) Hydrolysis Constants and Solubility of Chromium(III) Hydroxide. *Inorg. Chem.* **1986**, *26*, 345–349.
(28) Trudinger, P. A.; Chambers, L. A.; Smith, J. W. Low-Temperature Sulphate Reduction: Biological versus Abiological. *Can. J. Earth Sci.* **1985**, *22*, 1910–1918.
(29) Parbs, A.; Ebert, M.; Dahmke, A. Einfluss der Mineralpräzipitation auf die Funktionalität und Langzeiteffektivität von Fe0-Reaktionswänden—Ein Review anhand von 19 Fe0-Reaktionswandstandorten. *Grundwasser* **2007**, *12*, 267–281.
(30) Melitas, N.; Chuffe-Moscoso, O.; Farrell, J. Kinetics of Soluble Chromium Removal from Contaminated Water by Zerovalent Iron Media: Corrosion Inhibition and Passive Oxide Effects. *Environ. Sci. Technol.* **2001**, *35*, 3948–3953.
(31) Schlicker, O.; Ebert, M.; Fruth, M.; Weidner, M.; Wüst, W.; Dahmke, A. Degradation of TCE with Iron: the Role of Competing Chromate and Nitrate Reduction. *Ground Water* **2000**, *38*, 403–409.
(32) Furukawa, Y.; Kim, J.-W.; Watkins, J.; Wilkin, R. T. Formation of Ferrihydrite and Associated Iron Corrosion Products in Permeable Reactive Barriers of Zero-Valent Iron. *Environ. Sci. Technol.* **2002**, *36*, 5469–5475.
(33) Grolimund, D.; Senn, M.; Trottmann, M.; Janousch, M.; Bonhoure, I.; Scheidegger, A. M.; Marcus, M. Shedding New Light on Historical Metal Samples Using Micro-focused Synchrotron X-ray Fluorescence and Spectroscopy. *Spectrochim. Acta* **2004**, *59*, 1627–1635.

ES803526G